

Sb Ultra-Small Nanoparticles Embedded within N, S co-Doped Flexible Carbon Nanofiber Films with Longitudinal Tunnels as High Performance Anode Materials for Sodium-Ion Batteries

Jie You,^[a] Hongran Sun,^[a] Xiaojun Wang,^[a] Mai Li,^[a] Jingrui Sun,^[a] Peng Wang,*^[a] Yan He,^[a] and Zhiming Liu*^[a, b]

Designing low-cost carbon-based anode with excellent electrochemical performance plays a vital role in the commercialization of sodium-ion batteries (SIBs). However, its limited theoretical specific capacity and poor rate performance seriously affect its practical applications. Simply adjusting the morphological structure or component-based regulation strategies cannot usually solve all problems efficiently. In response, one-dimensional Sb₂S₃ nanorods with the longitudinal distribution are used as a sacrificial template in this work by a simple electrostatic spinning method. After heat treatment, abundant longitudinal distribution channels within flexible carbon nanofibers are obtained. Meanwhile, Sb ultra-small nanoparticles can be in-situ embedded within N, S co-doped carbon matrix (N,S,Sb-CNFs). Owing to the N, S, Sb co-modification and the

well-designed one-dimensional mesoporous carbon substrate, the N,S,Sb-CNFs hybrids achieve better interfacial contact with electrolyte, ameliorated electrical conductivity and distinct kinetic promotion. Furthermore, the undesired volume expansion of Sb nanoparticles during sodiation can also be efficiently suppressed. As expected, the N,S,Sb-CNFs based half-cell remains a reversible capacity of 287.8 mAh g⁻¹ at 1 A g⁻¹ even after 3500 cycles and harvests a capacity of 239.6 mAh g⁻¹ at a high current density of 4 A g⁻¹, demonstrating excellent cycling stability and rate performance. Furthermore, the assembled flexible full-cell matched with the Na₃V₂(PO₄)₂O₂F cathode also obtains superior bending resistance and continuous discharge ability during the deformation process, proving the potential of the flexible N,S,Sb-CNFs electrode in practical applications.

Introduction

The massive global consumption of fossil energy and the continuous environmental degradation have prompted scientists to turn their attention to renewable energy sources, the main examples of which are wind, solar, and tidal energy.^[1] The use of high performance energy storage devices to address the seasonality, locality and discontinuity of clean energy is essential for the efficient use of renewable energy. Low cost and long cycle life sodium-ion batteries are considered as a promising option in this field.^[2,3] Moreover, the anode materials are used in lithium-ion batteries, such as carbon materials, metals/alloys, and metal oxides/sulfides, can be optimized and

be applied to sodium-ion batteries. Among them, carbon materials have great potential for commercialization as an economical, easily preparing, and environmentally friendly electrode materials.^[4-8]

For thermodynamic reasons, graphite is not applicable in sodium-ion batteries, but carbon materials such as hard carbon, biomass carbon, and heteroatom-doped carbon are successfully applied in sodium ion batteries.^[9] Sodium storages in these carbon materials are achieved by sodium adsorption in cavities and gaps, sodium ion intercalation between carbon layers and adsorption by functional groups/defective sites.^[6,10-12] Specially, heteroatom modified carbon materials can significantly improve the low diffusion kinetics of bulk carbon materials, reflect the characteristics of capacitance control, and obtain better electrochemical performance at higher current densities to meet the requirements of large energy storage plants.^[13] The atomic size and electronegativity of the doping element affect the lattice changes and the electronic structure of the adjacent carbon atoms in carbon materials. For instance, the nitrogen-doped pyridine and pyrrole conformations can effectively increase the hydrophilicity and the specific capacitance as a result of the presence of lone-pair electrons and the redox reaction of N atoms.^[14-17] Sulfur doping can change the lattice spacing of carbon materials and results in a larger specific surface area.^[18-22] In addition, sulfur atoms are more likely to replace pyrrole nitrogen, creating a synergistic effect of nitrogen-sulfur co-doping.^[23,24] Except for the heteroatoms doping,

[a] J. You, H. Sun, Prof. Dr. X. Wang, M. Li, J. Sun, Prof. Dr. P. Wang, Prof. Dr. Y. He, Prof. Dr. Z. Liu
College of Electromechanical Engineering
Shandong Engineering Laboratory for Preparation and Application of High-Performance Carbon-Materials
Qingdao University of Science & Technology
Qingdao 266061 (PR China)
E-mail: pengwangmse@qust.edu.cn
zmliu@qust.edu.cn

[b] Prof. Dr. Z. Liu
Qingdao Industrial Energy Storage Research Institute
Qingdao Institute of Bioenergy and Bioprocess Technology
Chinese Academy of Sciences
Qingdao 266101 (China)

 Supporting information for this article is available on the WWW under
<https://doi.org/10.1002/batt.202300022>

the introduction of alloy-type anode materials such as Sb in carbon materials are reported to be beneficial to alleviate the huge volume expansion of alloy reactions, and the achieved Sb/carbon composites with optimized structure obtain stable cycling performance and higher energy density.^[25–27] Furthermore, previous researches have focused on the morphology modulation and combination form of Sb with conductive carbon materials, ignoring the optimization of carbon material matrices. In addition to being conductive and buffering materials, the carbon matrix can also be used as an excellent conductor and active host material for sodium ions by rational optimization of its microstructure.^[28,29]

Herein, we have designed a method for the synthesis of N, S and Sb ultra-small nanoparticles co-modified mesoporous carbon fibers. In detail, the one-dimensional Sb₂S₃ nanorods function as pore-forming template and Sb/S sources are first distributed longitudinally in the spun fibers during electrostatic spinning. Then after rational heat treatment, Sb₂S₃ is reduced by the carbon formed by PAN carbonization and transformed into numerous Sb ultra-small nanoparticles with an average diameter of 10 nm, which are closely embedded within N, S co-doped carbon nanofiber matrix. Also of interest is that during this high temperature calcination, the pyrolysis of Sb₂S₃ nanorods with longitudinal distribution orientation brings about abundant longitudinal tunnels within carbon skeleton, which increase the contact area between the carbon material and the electrolyte. As expected, the optimized carbon nanofibers modified by N, S co-doping and Sb ultra-small nanoparticles provide abundant active sites and the thus-achieved pore structures are beneficial for shortening the Na⁺ diffusion distance. These are critical factors for the much improved long-period cycling stability and rate performance of N,S,Sb-CNFs hybrids in comparison to that of pure CNFs. As a result, the half-cell assembled with N,S,Sb-CNFs remains a reversible capacity of 300 mAh g⁻¹ at 1 A g⁻¹ even after 3500 cycles and harvests a superior capacity of 239.6 mAh g⁻¹ at a high current density of 4 A g⁻¹, indicating that the deliberately designed N,S,Sb-CNFs composite demonstrates great potential for practical applications in sodium-ion batteries.

Results and Discussion

Microstructure characterization

Figure 1 illustrates the synthesis process of N,S,Sb-CNFs in which one-dimensional Sb₂S₃ nanorods are selectively removed as sacrificial templates to form widely distributed Sb ultra-small nanoparticles embedded within N, S co-doped flexible carbon nanofiber films with longitudinal tunnels. Scanning electron microscopy (SEM) and transmission electron microscopy (TEM) are used on N,S,Sb-CNFs and pure CNFs to demonstrate their structural characteristics. As shown in Figure 2(a), the carbon fiber still maintains a good one-dimensional shape with a diameter distribution between 500 nm and 1 μm, and the SEM image of the cross-section (Figure 2b) shows that it has a rich pore structure inside. In contrast, the pure CNFs (Figure S1) has a smoother surface and no channels can be distinguished in the cross-sectional SEM, which is typical of the 1D carbon fiber shape. Figure 2(d and e) show the N,S,Sb-CNFs strategically exhibiting an abundance of longitudinal pores at the expense of the template, and the pores within the fiber can be clearly observed in the cross-sectional TEM extending all the way through the section. The rich pore structure inside the fiber will inevitably increase the contact area between the electrolyte and the carbon material, thus optimizing the diffusion kinetics of sodium ions. From the Figure S2(a, b), it can be seen that Sb ultra-small nanoparticles are uniformly distributed in the carbon fibers. Energy dispersive X-ray (EDX) spectra of N,S,Sb-CNFs indicate the presence of C,N,S and Sb in the carbon fibers in Figure S3. And the corresponding selected element distribution (Figure 2f) can be observed as a uniform distribution of Sb ultra-small nanoparticles and S doping in the carbon matrix, which is attributed to the modification of the carbon substrate by Sb₂S₃ during the carbon thermal reduction process. Furthermore, it is of interest that the PAN forms N-doping during the carbonization process, which further increases the electrical conductivity of the carbon substrate. Furthermore, the high-resolution TEM (HRTEM) images are used to further characterize the presence of Sb in the carbon matrix. Figures 2(c) and S4 show the presence of lattice stripes in the amorphous carbon matrix in dispersed regions of a few nanometers to tens of nanometers. The calculated spacing of

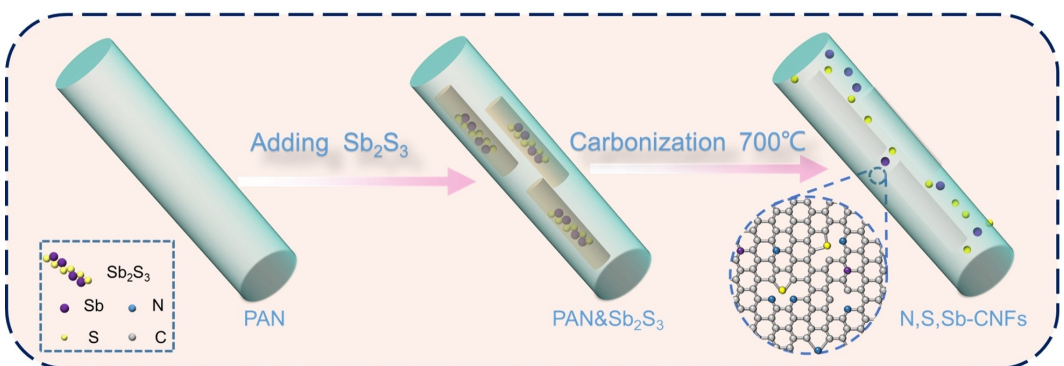


Figure 1. Preparation process and mechanism of N,S,Sb-CNFs.

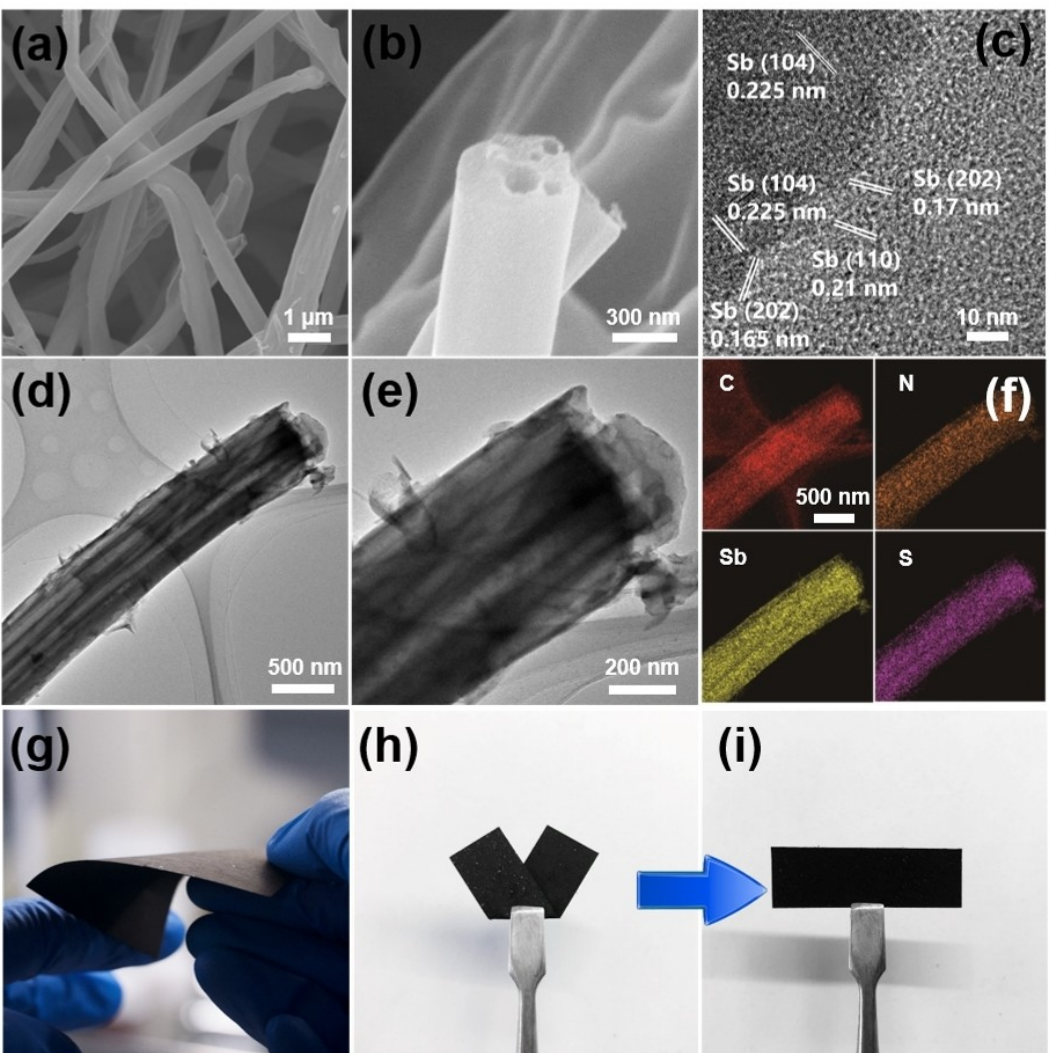


Figure 2. a) SEM image of N,Sb-CNFs. b) Cross-sectional view of N,Sb-CNFs. c) HRTEM image of N,Sb-CNFs. d, e) TEM images of N,Sb-CNFs at different magnifications. f) TEM mapping image of N,Sb-CNFs. g–i) Optical photo of N,Sb-CNFs.

the lattice stripes are about 0.17 nm, 0.21 nm and 0.225 nm, which correspond to the (202), (110) and (104) crystallographic planes of Sb, respectively. This confirms the uniform embedding of Sb ultra-small nanoparticles in the carbon matrix. More noteworthy is that, as shown in Figure 2(g and h), the N,Sb-CNFs film can be smoothly bent and folded without crack and fracture, demonstrating its outstanding flexibility.^[30,31] Furthermore, Figure 2(i) shows the optical image of the N,Sb-CNFs film after bending and folding. It can be clearly seen that the fiber film is well recovered and did not appear creases, which reflects its excellent application prospect in high-efficiency self-supporting sodium-ion battery electrodes.

Structure properties analysis

We also performed comparative characterization of hollow carbon and pure carbon materials by X-ray diffraction (XRD), Raman spectroscopy (Raman) and X-ray photoelectron spectro-

scopy (XPS), respectively. Both N,Sb-CNFs and pure CNFs in XRD tests (Figure 3a) exhibit characteristic peaks of amorphous carbon, and the absence of characteristic peaks of Sb can be clearly observed by comparing standard cards. This is due to the distribution of ions and metallic antimony (Sb) in the carbon fibers in the form of ultra-small nanoparticles. It can be noted that the mesoporous carbon shows a broader and flatter amorphous carbon peak (~26°), presumably due to the interlayer expansion caused by the doping of S and N elements with the embedding of Sb ultra-small nanoparticles and the formation of tile-like nanosheets with curled edges, as demonstrated in previous reports.^[32–34] In order to verify the difference of the degree of amorphous carbon material, Raman (Figure 3b) is used to test the N,Sb-CNFs and pure CNFs, and the ratio of I_D/I_G of the fitted mesoporous carbon was 1.44 and 1.31, respectively. The larger value of I_D/I_G proves that the degree of amorphous carbon fiber of N,Sb-CNFs is larger than that of pure CNFs, which is beneficial to increase the additional sodium storage sites of carbon material and make the carbon material

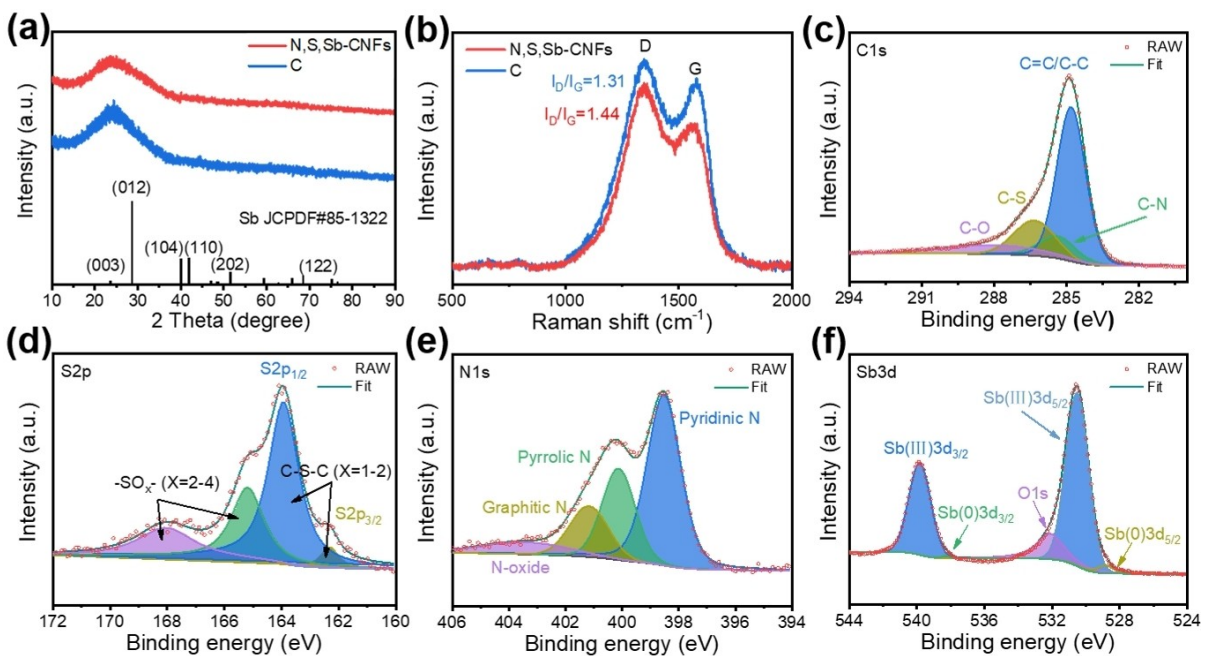


Figure 3. a) XRD patterns of N,Sb-CNFs and pure CNFs. b) Raman spectra of N,Sb-CNFs and pure CNFs. c-f) XPS spectra of N,Sb-CNFs.

obtain a higher specific capacity. It can be seen that S, N co-doping and Sb ultra-small nanoparticles do cause a change in the degree of amorphous carbon fiber. To further determine the connection between S, N and Sb and C material, we characterize the mesoporous carbon material by XPS. The survey spectra proves the presence of Sb, C, N, and S elements in Figure S5. The elemental fine spectrum of C 1s is shown in Figure 3(c). C 1s is carefully divided into four peaks. 284.8 eV of the peak is assigned to the C=C/C-C bond, 285.29 eV is assigned to the binding energy of C-N bond, 286.39 eV is identified as the position of the binding energy of C-S bond, and 288.59 eV is around the position of C-O bond. The analysis of the elemental fine pure of C 1s verifies that S, N elements are both to be bonded to C.^[35] To verify the presence of S and N forms, we also analyzed the fine spectra of S 2p and N 1s (Figure 3d and e).^[34] The fine spectra of S 2p obtained by fitting the split peaks at 162.29 eV and 163.89 eV correspond to thiophene-S C-S-C ($X=1-2$) as S 2p_{3/2} and S 2p_{1/2}, respectively, due to the spin-orbit coupling. 165.19 eV and 168.09 eV are attributed to sulfate or sulfonate ($-SO_x$, $X=2-4$).^[36] The fine spectral analysis of the N element can be observed that it can be divided into four peaks, 398.59 eV, 400.19 eV, 401.19 eV for pyridine nitrogen, pyrrole nitrogen and graphite nitrogen, respectively, and 403.69 eV is assigned to nitrogen oxides.^[34] Among them, pyridine nitrogen and pyrrole nitrogen can endow the carbon skeleton with abundant external defects and active sites and improve the overall electrical conductivity of the carbon layer thus improving the sodium storage properties. As shown in Figure 3f, the elemental fine spectrum of Sb partially overlaps with the O 1s spectrum, and Sb has the main two peaks at 530.39 eV and 539.79 eV, which are attributed to the presence of trivalent Sb (3d_{5/2} and 3d_{3/2}) due to the partial oxidation of the Sb surface. The two weak peaks at 538.29 eV

and 528.79 eV correspond to 3d_{5/2} and 3d_{3/2} of zero-valent Sb, respectively, which proves the mosaic of Sb in the carbon matrix.^[37,38] Then, thermo-gravimetric analysis (TGA) was performed to determine the content of Sb in the N,Sb-CNFs sample. According to the TGA profile in Figure S6, the mass contents of Sb in N,Sb-CNFs is determined as 10.44 wt%. The carbon matrix has abundant defects and voids after elemental doping and in situ embedding of Sb ultra-small nanoparticles, which facilitates the electrolyte penetration to accelerate the kinetics of sodium storage and desodiation.

Electrochemical properties

To evaluate the sodium storage capacity of the prepared samples, a CR2032 button cell with sodium foil as counter electrode was assembled.^[39] CV (0.01–2.0 V) tests were first performed at 0.1 mVs⁻¹ to observe the detailed electrochemical behavior. As shown in Figure 4(a), during the first cycle of cathodic sweep, there is a significant reduction peak at 0.802 V, which corresponds to the formation of Na_xSb during the initial sodiation process and the generation of SEI films. During the second cycle of cathode scanning, two new peaks appeared at 0.719 V and 0.25 V, corresponding to the two-step alloying reaction of Sb, resulting in the intermediate Na_xSb and the final Na₃Sb alloy, respectively. In the anodic scanning process, two oxidation peaks appear at 0.721 V and 1.297 V, which correspond to the transformation from Na₃Sb to the intermediate Na_xSb and the recovery of Sb by dealloying reaction, respectively.^[39–41] The stepwise alloying-dealloying reactions of N,Sb-CNFs during redox process can be summarized as following:

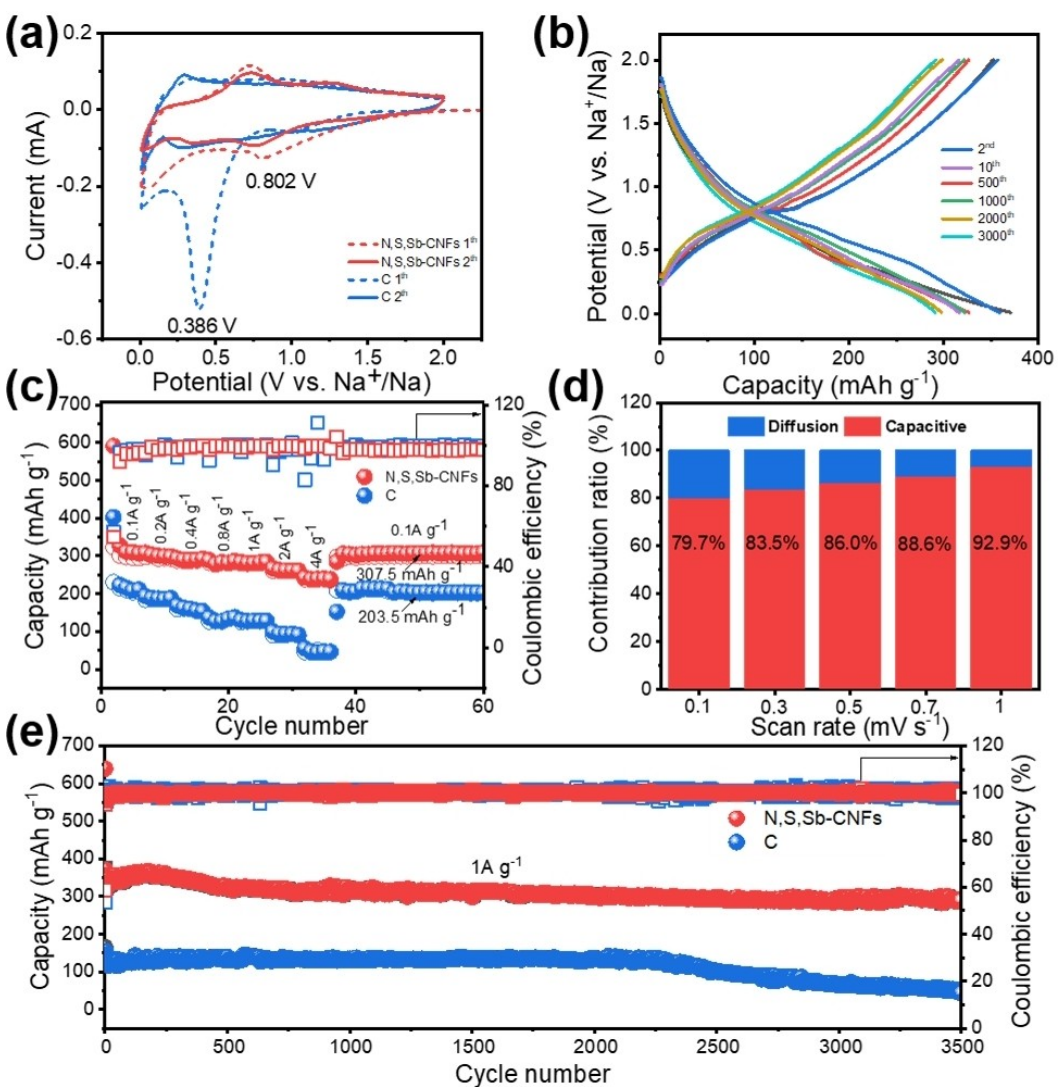
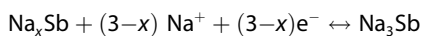
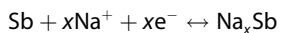


Figure 4. Electrochemical performance of N,Sb-CNFs in SIBs. a) CV curves of N,Sb-CNFs and pure CNFs for the first 2 cycles at 0.1 mV s^{-1} . b) GCD curves of N,Sb-CNFs for different cycles at 1 A g^{-1} . c) Rate performance of N,Sb-CNFs and pure carbon fiber at various current densities. d) The percentage of the capacitive contribution of N,Sb-CNFs at different scan rates. e) Cycling performance at 1 A g^{-1} for N,Sb-CNFs and pure CNFs.



It is mentioned that as shown in Figure S7(a), the reduction and oxidation peaks remains unchanged in the subsequent scans, showing high reversibility and stability. In sharp contrast, the first scan of pure carbon (Figure S7b) shows a strong anodic peak at 0.386 V , which corresponds to the formation of SEI. The anodic scan has no obvious peaks, which proves that the difference with the N,Sb-CNFs is the pure CNFs does not have the occurrence of alloying and de-alloying reactions of Sb, which is one of the reasons for the higher specific capacity of the mesoporous carbon material. It can be observed in Figure S7(c, d) (Supporting Information) that the plateau appearing in the charge-discharge curve can correspond to the peak in the CV, and the charge-discharge curves can overlap together except for the first turn, which shows the good cycling

stability of the N,Sb-CNFs. Figure 4(b) compares the charge/discharge curves of the mesoporous carbon electrode under different cycle turns, and shows that the charge/discharge curve of the 2nd cycle until the 3000th cycle can keep the shape of the plateau well and overlap well, which proves that the N,Sb-CNFs has excellent cycling stability.

In order to verify the effects of mesoporous and elemental doping and inlay on the sodium storage performance of the material, the rate performance and cycling performance of mesoporous carbon material and pure carbon material are tested and analyzed separately. N,Sb-CNFs show better specific capacity than pure CNFs at all rates (Figure 4c). The mesoporous carbon material electrode exhibits the best rate performance with delivering average specific discharge capacities of $310.1, 303.3, 290.4, 282.3, 282, 261.9$ and 239.6 mAh g^{-1} at $0.1, 0.2, 0.4, 0.8, 1, 2$ and 4 A g^{-1} , respectively. It is higher than those of pure CNFs at $223, 188.8, 160.2, 127.7, 127.4, 93.4$ and 45.6 mAh g^{-1} for pure CNFs. And the N,Sb-CNFs could

recover to 307.5 mAhg⁻¹ when the current density returns to 0.1 Ag⁻¹, which proved that the N, S-doped and Sb ultra-small nanoparticles embedded N,Sb-CNFs could maintain their microstructures before and after cycling.

To better understand the kinetic behavior of N,Sb-CNFs sodium-ion batteries, the electrochemical impedance spectra (EIS) of the pristine and 10th cycled electrodes are analyzed. As shown in Figure S8(a), the Nyquist diagram consists of a semicircle in the high frequency region and a straight line in the low frequency region. The semicircle in the high frequency region is attributed to the charge transfer resistance (R_{ct}) and the straight line in the low frequency region is corresponding to the impedance of the diffusion process. It can be seen that the diameter of the semicircles in the high frequency region for the pristine N,Sb-CNFs electrode is much smaller than that of pure C electrode, indicating that N,Sb-CNFs benefits fast charge transfer across the electrode/electrolyte interface. More importantly, the R_{ct} value of the 10 cycled N,Sb-CNFs electrode manifest a distinct advantage in comparison to that of pure C electrode, further demonstrating its outstanding kinetic performance (Figure S8b). Then, we performed CV tests on mesoporous carbon materials with different scan speeds and observed two cathodic peaks at 0.7 V, 0.4 V and an anodic peak at 0.8 V. The data from the peak positions are fitted to obtain b values of 0.924, 0.995 and 0.876, respectively. According to Equation (1):

$$i = av^b \quad (1)$$

where i is the peak current, v is the scan rate, a and b are empirical parameters, and the value of b can vary between 0.5 and 1. When b is close to 1, the electrochemical process is mainly controlled by interfacial reactions or capacitive charge storage; b close to 0.5 is typical for diffusion control process, which is a typical diffusion-limited process.^[42-44] Therefore, the b value of N,Sb-CNFs exhibits a typical surface-controlled reaction, indicating fast interfacial charge storage kinetics of Na ions. To further analyze the control of surface capacitance, the relationship between peak current (i) and potential (V) can be described by the following Equation (2):

$$i(V) = k_1v + k_2v^{1/2} \quad (2)$$

where k_1v represents the capacitive control and $k_2v^{1/2}$ represents the diffusion control. k_1 and k_2 are variable parameters that can be fitted by $i(V)$, $v^{1/2}$ and the graph. Thus, the percentage of capacitive contribution at 0.1, 0.3, 0.5, 0.7 and 1 mVs⁻¹ sweep rates can be calculated by k_1 and k_2 .

It can be seen in Figures 4(d) and S9 that the capacitance contribution percentage is 79.7% at 0.1 mVs⁻¹ and grows to 92.9% at 1 mVs⁻¹. Due to the existence of longitudinal pore channels, N,S co-doping and the presence of Sb ultra-small nanoparticles, the rapid sodium storage kinetics of N,Sb-CNFs is controlled by surface capacitance instead of Faraday reaction. The capacitance control gradually increases with the increase of scan speed, indicating that the contribution of rapid interfacial reaction increases at high scan speed. The high

current density cycling test (Figure 4e) is performed on mesoporous carbon material and pure carbon material. In this work, the N,Sb-CNFs were cut into 10 mm diameter pieces for directly using as self-supporting anode to assemble half batteries. The discharge and charge capacities were determined by considering the whole mass of the N,Sb-CNFs piece. Figure 4(e) shows that N,Sb-CNFs have an initial capacity of 376.5 mAhg⁻¹ compared to only 165.6 mAhg⁻¹ for pure CNFs. The capacity of mesoporous carbon material remains to 287.8 mAhg⁻¹ after 3500 cycles of charging and discharging compared to less than 50 mAhg⁻¹ for pure CNFs. After 3500 cycles, the capacity retention rate of N,Sb-CNFs is 76.5%, while the capacity retention rate of pure CNFs in the comparison sample was only 27.1%, which shows better capacity retention at high currents due to its large contact area with electrolyte and high electrical conductivity. After 3500 cycles, the capacity retention rate of N,Sb-CNFs is 76.5%, while the capacity retention rate of pure CNFs in the comparison sample was only 27.1%, which shows better capacity retention at high currents due to its large contact area with electrolyte and high electrical conductivity. In summary, the overall electrochemical performances of N,Sb-CNFs are comparable to many recently reported carbon materials loaded with Sb components for sodium ion batteries (Supporting Information Table S1). It can be inferred that the carbon nanofibers modified with N,S co-doping and Sb ultra-small nanoparticles in this work benefit enriching the active sites and enhancing mass transfer efficiency. This plays a crucial role in providing N,Sb-CNFs with superior long-term cycling stability and significantly improved rate performance.

In order to analyze the reaction mechanism of sodium ions in N,Sb-CNFs, we performed ex-situ HRTEM tests to elucidate the changes in Sb during sodiation/desodiation.^[45] Figure 5(a) shows that when N,Sb-CNFs are discharged to 0.01 V in the first time, nanodots with the structural characteristics of the Na₃Sb lattice can be observed in the carbon matrix, with a spacing of 0.186 nm that can be attributed to the (006) crystal plane or the (114) crystal plane of Na₃Sb, and 0.237 nm that corresponds well to the (200) crystal plane of Na₃Sb. The corresponding SAED pattern (Figure 5b) corresponds better to the above results. It is clear that Sb underwent an alloying reaction with sodium ions to produce the Na₃Sb phase as the final sodium product present. When the N,Sb-CNFs are charged to 2.0 V (Figure 5c), the HRTEM shows lattice spacings of 0.231 nm, 0.214 nm and 0.177 nm corresponding to the (104), (110) and (202) crystal planes of Sb, respectively. Figure 5(d) also confirms the presence of Sb, which can correspond to the (011), (104), (110), (017), (202) and (124) Sb crystal planes. The reversible alloying drawing and de-alloying reaction processes of Sb in N,Sb-CNFs were confirmed by ex-situ HRTEM tests during charging and discharging as described above.^[16,46] Further sodiation/ desodiation of N,Sb-CNFs were observed using TEM images and corresponding elemental mapping images. Figure 5(e, f) show TEM images of N,Sb-CNFs in different states. When fully discharged to 0.01 V (Figure 5e), smooth and intact fibers can be observed, indicating that the formation of Na₃Sb by the alloying reaction of Sb

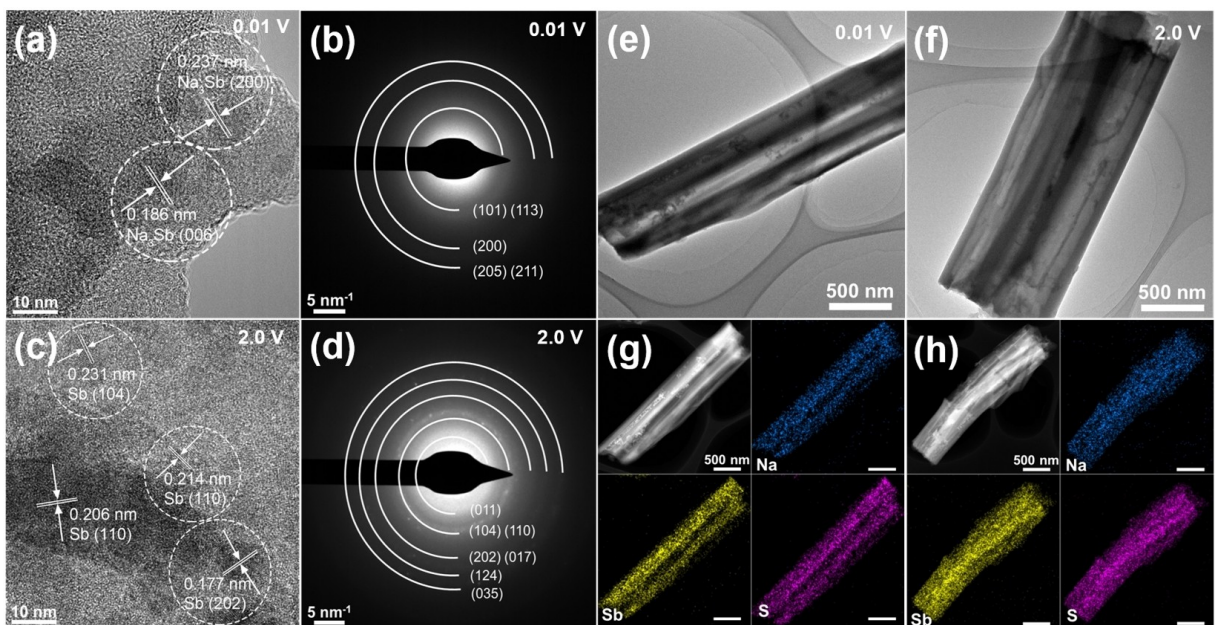


Figure 5. a, c) Ex situ HRTEMs images and b, d) SAED images of N,Sb-CNFs at 0.01 V and 2.0 V. e, f) TEM images and g, h) element mapping images of N,Sb-CNFs for the first cycle after a full discharge and full charge.

during the sodiation process did not cause significant volume expansion to collapse the fiber structure, further explaining that the reaction of Sb ultra-small nanoparticles in the fibers with sodium ions to form Na_3Sb alloying compounds was not sufficient to destroy the fibers supported by the hollow structure, thus the structural integrity was maintained. The uniform distribution of Na_3Sb in the carbon matrix can be observed through the dark field images and elemental mapping images in Figure 5(g). When the N,Sb-CNFs are fully charged to 2.0 V (Figure 5f), the carbon fibers are preserved intact. The uniform distribution of Sb in the carbon matrix can be observed in the dark field image and the elemental mapping image in Figure 5(h). The bright spots of Sb ultra-small nanoparticles can still be observed in the dark field image, which further illustrates the reversibility of the reaction. The stability of the structure before and after the charge-discharge reaction also provides evidence for the subsequent cycling stability during the charge-discharge process.^[47–49]

To further explore the potential of mesoporous carbon materials for practical applications and applications in flexible devices, we assembled CR2032 button full cells and flexible pack full cells using flexible $\text{Na}_3\text{V}_2(\text{PO}_4)_2\text{O}_2\text{F}$ electrodes (Figure 6a).^[36,50,51] The flexible cathode and flexible anode materials are first directly stamped into 10 mm diameter electrode sheets for full-cell assembly, which avoids the use of collector and increases the overall mass-to-capacity. The anode material is assembled in a half-cell before the full cell is assembled and pre-cycled for 5 turns before discharging to 0.01 V to allow the anode material to be fully embedded in sodium. As shown in Figure 6(b), the test voltage range of the full cell is 1.5–4.3 V. The platform shape of the charge/discharge curve of the full cell is a combination of the platform of the cathode material and the platform of the anode material, and its charging

process and discharging process demonstrate two charging and discharging platforms. Figure 6(c) shows the rate performance ($1 \text{ C} = 120 \text{ mA g}^{-1}$) and cycling performance of the button-type full cell, which is tested with the mass of the cathode material. The full battery demonstrated a specific capacity of 123.4, 114.9, 101, 88.5, 77, 68.1, 57.3, 48.5 mAh g^{-1} in the 1 C, 2 C, 3 C, 4 C, 5 C, 6 C, 8 C and 10 C rate tests, respectively. And the tested rate resumed at 1 C the full battery capacity returned to 110.7 mAh g^{-1} and continued at the 1 C rate the cycle stability is excellent for 60 cycles, and the capacity of 102.2 mAh g^{-1} was maintained at the 100th cycle. We have successfully assembled a soft pack battery using a flexible $\text{Na}_3\text{V}_2(\text{PO}_4)_2\text{O}_2\text{F}$ cathode and a flexible mesoporous carbon anode and tested the electrochemical performance of the soft pack battery in different states (flat-folded 90°-folded 180°-flat). Figure 6(d–f) show that the soft pack battery can continue to light LED beads when folded and recovered along the short side and Figure 6(g–i) show a pouch battery can still continuously light the LED lamp beads when folded along the long side and recovered. This demonstrates the potential of flexible mesoporous carbon electrodes that can be folded to suit different usage scenarios. In addition, as shown in Figure S10(a), we tested the flexible soft pack battery in different states (flat-bending $r=4 \text{ cm}$ -bending $r=2 \text{ cm}$ -flat), and the battery exhibited a specific capacity of about 80 mAh g^{-1} and remained stable in different states, and the charge/discharge curves (Figure S10b) collected in different states overlapped well. The cyclic stability and feasibility of the flexible $\text{Na}_3\text{V}_2(\text{PO}_4)_2\text{O}_2\text{F}$ positive electrode and the flexible mesoporous carbon anode electrode in the assembly of flexible sodium ion battery are verified by the test. The excellent cyclic stability can support the flexible sodium ion battery in flexible wearable devices and complex space applications.^[52–55]

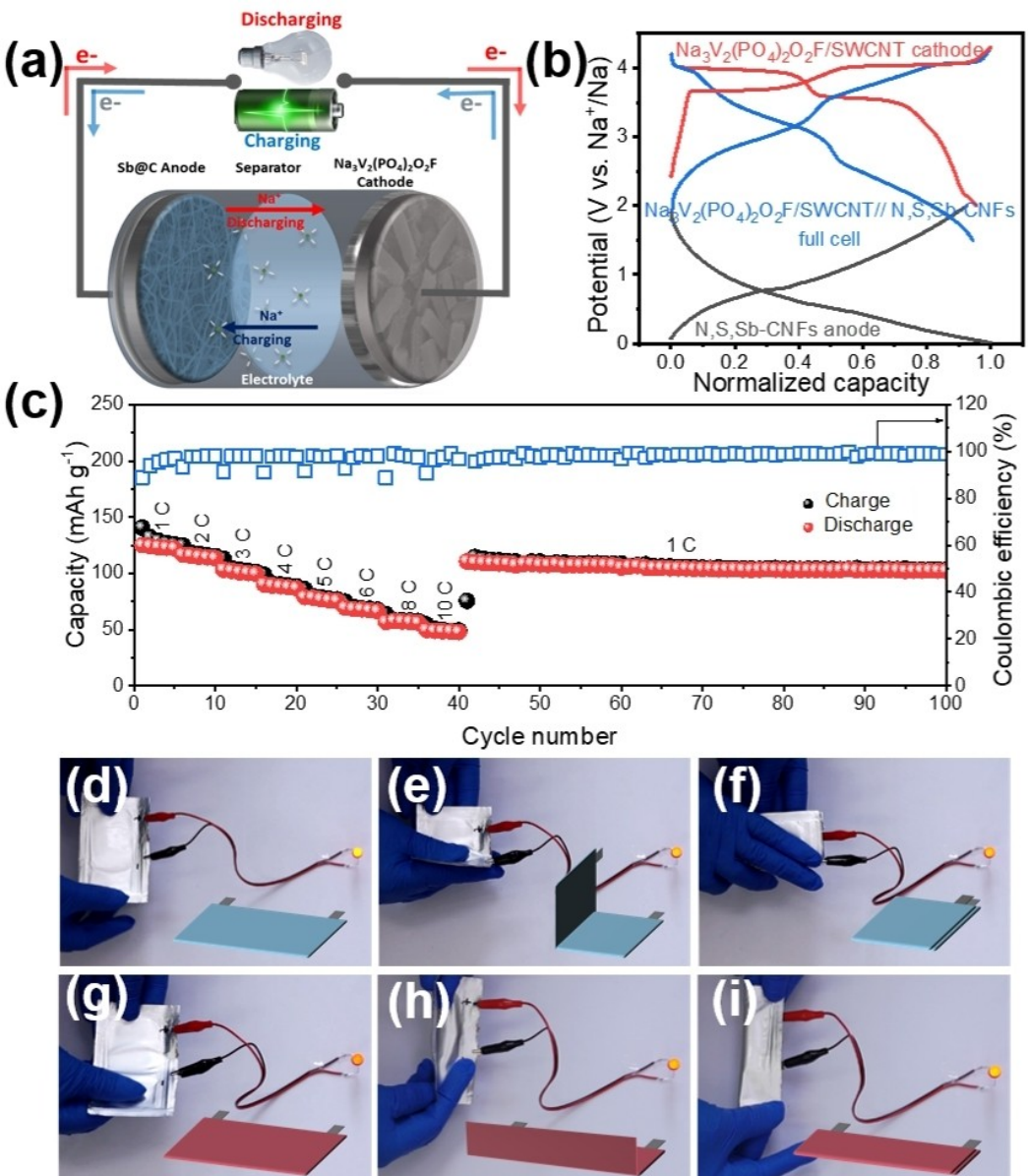


Figure 6. The Schematic illustration and performance of Na₃V₂(PO₄)₂O₂F | N,S,Sb-CNFs full cell. a) The Schematic illustration of Na₃V₂(PO₄)₂O₂F | N,S,Sb-CNFs full cell. b) GCD profiles of NVPOF cathode, N,S,Sb-CNFs anode in half cells, and Na₃V₂(PO₄)₂O₂F | N,S,Sb-CNFs sodium-ion full cell. c) Rate performance and cycling performance of the full cell. d-i) Bending test of the soft pack battery.

Conclusion

In summary, using one-dimensional Sb₂S₃ nanorods as sacrificial templates, we have obtained a free-standing flexible carbon nanofiber films with abundant longitudinally distributed pores by a simple electrostatic spinning method and the following heat treatment. Meanwhile, lots of Sb ultra-small nanoparticles can be successfully in-situ embedded within the N,S co-doped carbon nanofiber matrix. The thus optimized N,S,Sb-CNFs hybrid increases the contact area with the electrolyte, and the conductivity and kinetics of the carbon material due to the doping of N and S heteroatoms as well as the synergistic effect between Sb nanoparticles and the modified carbon substrate. On the one hand, the introduction of N,S co-doping and the

anchored Sb nanoparticles increase the amorphous degree of the carbon matrix. On the other hand, the increased amounts of N,S,Sb co-modified active sites in the carbon material contribute to improving the overall mass specific capacity. As expected, the full cells assembled with Na₃V₂(PO₄)₂O₂F cathode and N,S,Sb-CNFs anode show outstanding rate and cycling performance. Furthermore, the flexible full cell also obtains superior bending resistance and cycling performance, proving the practical application potential of the flexible N,S,Sb-CNFs hybrid in wearable devices in complex spaces.

Experimental Section

Materials preparation

Synthesis of the precursor Sb_2S_3

In a typical synthesis, first, $SbCl_3$, L-cysteine, $Na_2S \cdot 9H_2O$ with a stoichiometric molar ratio ($SbCl_3$: L-cysteine: $Na_2S \cdot 9H_2O = 4:8:8$ mmol) were orderly dissolved in 80 mL of deionized water. After magnetic stirring for 3 h, transferred the homogeneous suspension to a Teflon-lined stainless steel autoclave and maintained at 180 °C for 12 h for a hydrothermal reaction. After cooling naturally to room temperature, centrifuged and washed with deionized water and ethanol for several times, and dried under vacuum overnight at 60 °C.

Preparation of the N,S,Sb -CNFs

The spinning solution was formed by stirring 0.9 g PAN and 1.8 g DMF at 60 °C for 6 h. 1.35 g Sb_2S_3 one-dimensional nanorods were added into the spinning solution and stirred for 6 h at the same temperature to obtain a uniformly distributed spinning solution of one-dimensional Sb_2S_3 nanorods. The voltage of electrostatic spinning was set at 20 kV and the pushing glue speed was carried out 0.8 mL h⁻¹. The distance between the needle tip and the aluminum foil was set at 25 cm, and the composite fiber material was collected using a roller collection device covered with aluminum foil. The obtained composite fiber film was dried at 60 °C for 6 h and then transferred a tube furnace for calcination. Under air atmosphere, the temperature was initially increased at 2 °C min⁻¹ to 250 °C, held at 250 °C for 1 h, then ramped up to 700 °C at a rate of 5 °C min⁻¹ under an argon atmosphere and held for 6 h to form a carbon fiber electrode material with longitudinal pores of Sb ultra-small nanoparticles embedded within N, S codoped flexible carbon nanofiber films. Using a sheet press, the N,S,Sb -CNFs were cut into 10 mm diameter pieces for directly using as self-supporting anode electrode material.

Preparation of the cathode electrode

$Na_3V_2(PO_4)_2O_2F$ and carbon nanotubes were dissolved in DMF at a mass ratio of 7:3 in an ultrasonicator until uniformly dispersed. The dispersed dispersion was filtered with a vacuum filter to form a flexible film. Put the filtered flexible film into a vacuum drying oven and vacuum dry at 60 °C for 12 h.

Material characterization

Field emission scanning electron microscope (FESEM, Hitachi SU8010) and transmission electron microscope (TEM, FEI Talos 200S) were used to describe the morphology of the samples. XRD pattern (XRD) was recorded on a X-ray diffractometer (Rigaku MiniFlex) in the scan range (2θ) of 3°–90°. Raman spectra were examined from 500 to 2000 cm⁻¹ on a confocal Raman spectrometer (HORIBA LabRAM HR Evolution) with a 532 nm Ar ion laser. The valence and bonding forms of elements were characterized by X-ray photoelectron spectroscopy (XPS, Kratos Axis Supra).

Electrochemical measurements

Both the half-cell and full-cell tests were assembled into CR2032 coin cells. The separator was glass fiber (Whatman). Sodium metal was used as a counter electrode in half-cell tests. The electrolyte was 1.0 M sodium perchlorate ($NaClO_4$) in propylene carbonate

(PC) with 5 vol% of fluoroethylene carbonate (FEC) additive. Both half-cell and full-cell electrostatic charging/discharge tests were performed on the LAND CT2001 A battery test system. The potential window of the half-cell was set to 0.01–2.0 V vs. Na^+/Na . The full battery potential window was 2.0–4.3 V vs. Na^+/Na . The potential window for cyclic voltammetry (CV) tests was set to 0.01–2 V, and the frequency range for electrochemical impedance spectroscopy (EIS) tests was 0.01–100 kHz. Both tests were performed on an electrochemical workstation (IVIUM, V46808). Before the full battery assembly test, the anode underwent a presodiation process where the electrode material was cycled five times at a current density of 0.1 A g⁻¹ and then disassembled in a glove box (Mikrouna). The matching ratio of anode /cathode capacity was about 110%. The soft pack full battery was assembled in the glove box in the same way.

Acknowledgements

This work was funded by the National Natural Science Foundation of China (Grant Nos. 21905152, 52176076, and 22005167), the Youth Innovation Team Project for Talent Introduction and Cultivation in Universities of Shandong Province, the Taishan Scholar Project of Shandong Province of China (Grant Nos. tsqn202211160 and ts20190937), the China Postdoctoral Science Foundation (Grant Nos. 2022M713249, 2021M693256 and 2021T140687), and the Shandong Provincial Natural Science Foundation of China (Grant Nos. ZR2020QB125).

Conflict of Interest

The authors declare no conflict of interest.

Data Availability Statement

The data that support the findings of this study are available from the corresponding author upon reasonable request.

Keywords: antimony • N,S,Sb -CNFs • longitudinal tunnels • sodium-ion batteries • electrochemical performance

- [1] T. M. Gür, *Energy Environ. Sci.* **2018**, *11*, 2696–2767.
- [2] P. Albertus, S. Babinec, S. Litzelman, A. Newman, *Nat. Energy* **2017**, *3*, 16–21.
- [3] Y. Fang, X.-Y. Yu, X. W. Lou, *Matter* **2019**, *1*, 90–114.
- [4] P. K. Nayak, L. Yang, W. Brehm, P. Adelhelm, *Angew. Chem. Int. Ed.* **2018**, *57*, 102–120; *Angew. Chem.* **2018**, *130*, 106–126.
- [5] M. Wang, Q. Wang, X. Ding, Y. Wang, Y. Xin, P. Singh, F. Wu, H. Gao, *Interdiscip. Mater.* **2022**, *1*, 373–395.
- [6] M. Lao, Y. Zhang, W. Luo, Q. Yan, W. Sun, S. X. Dou, *Adv. Mater.* **2017**, *29*, 170062.
- [7] C. Ma, T. Xu, Y. Wang, *Energy Storage Mater.* **2020**, *25*, 811–826.
- [8] L. Shen, Y. Wang, F. Wu, I. Moudrakovski, P. A. van Aken, J. Maier, Y. Yu, *Angew. Chem. Int. Ed.* **2019**, *58*, 7238–7243; *Angew. Chem.* **2019**, *131*, 7316–7321.
- [9] Z. Y. Gu, J. Z. Guo, J. M. Cao, X. T. Wang, X. X. Zhao, X. Y. Zheng, W. H. Li, Z. H. Sun, H. J. Liang, X. L. Wu, *Adv. Mater.* **2022**, *34*, e2110108.
- [10] W. T. Jing, C. C. Yang, Q. Jiang, *J. Mater. Chem. A* **2020**, *8*, 2913–2933.
- [11] J.-M. Ma, Y.-T. Li, *Rare Met.* **2020**, *39*, 967–969.

- [12] M. C. Schulze, R. M. Belson, L. A. Kraynak, A. L. Prieto, *Energy Storage Mater.* **2020**, *25*, 572–584.
- [13] D.-S. Liu, D.-H. Liu, B.-H. Hou, Y.-Y. Wang, J.-Z. Guo, Q.-L. Ning, X.-L. Wu, *Electrochim. Acta* **2018**, *264*, 292–300.
- [14] J. Ge, L. Fan, J. Wang, Q. Zhang, Z. Liu, E. Zhang, Q. Liu, X. Yu, B. Lu, *Adv. Energy Mater.* **2018**, *8*, 1801477.
- [15] L. Ma, M. Cao, C. s. Zhao, S. Huang, J. Ding, J. Chen, Y. Zhou, *Ceram. Int.* **2021**, *47*, 9118–9124.
- [16] W. T. Jing, Y. Zhang, Y. Gu, Y. F. Zhu, C. C. Yang, Q. Jiang, *Matter* **2019**, *1*, 720–733.
- [17] W. Shen, C. Wang, Q. Xu, H. Liu, Y. Wang, *Adv. Energy Mater.* **2015**, *5*, 1400982.
- [18] Z. Hong, Y. Zhen, Y. Ruan, M. Kang, K. Zhou, J. M. Zhang, Z. Huang, M. Wei, *Adv. Mater.* **2018**, *30*, e1802035.
- [19] P. Bai, Y. He, X. Zou, X. Zhao, P. Xiong, Y. Xu, *Adv. Energy Mater.* **2018**, *8*, 1703217.
- [20] Y. Qian, Y. Li, Z. Yi, J. Zhou, Z. Pan, J. Tian, Y. Wang, S. Sun, N. Lin, Y. Qian, *Adv. Funct. Mater.* **2020**, *31*, 2006875.
- [21] P. Geng, S. Zheng, H. Tang, R. Zhu, L. Zhang, S. Cao, H. Xue, H. Pang, *Adv. Energy Mater.* **2018**, *8*, 1703259.
- [22] Y. Li, J. Qian, M. Zhang, S. Wang, Z. Wang, M. Li, Y. Bai, Q. An, H. Xu, F. Wu, L. Mai, C. Wu, *Adv. Mater.* **2020**, *32*, e2005802.
- [23] Q. Jin, K. Wang, P. Feng, Z. Zhang, S. Cheng, K. Jiang, *Energy Storage Mater.* **2020**, *27*, 43–50.
- [24] C. Ding, L. Huang, J. Lan, Y. Yu, W. H. Zhong, X. Yang, *Small* **2020**, *16*, e1906883.
- [25] K.-X. Lei, J. Wang, C. Chen, S.-Y. Li, S.-W. Wang, S.-J. Zheng, F.-J. Li, *Rare Met.* **2020**, *39*, 989–1004.
- [26] S. Jena, A. Mitra, S. Das, D. Das, K. Das, S. B. Majumder, S. Das, *Appl. Surf. Sci.* **2021**, *542*, 148756.
- [27] J. Yang, X. Zhou, D. Wu, X. Zhao, Z. Zhou, *Adv. Mater.* **2017**, *29*, 1604108.
- [28] Y. Fang, D. Luan, X. W. D. Lou, *Adv. Mater.* **2020**, *32*, e2002976.
- [29] Y. Fang, X. Y. Yu, X. W. D. Lou, *Angew. Chem. Int. Ed.* **2018**, *57*, 9859–9863; *Angew. Chem.* **2018**, *130*, 10007–10011.
- [30] B. H. Hou, Y. Y. Wang, Q. L. Ning, W. H. Li, X. T. Xi, X. Yang, H. J. Liang, X. Feng, X. L. Wu, *Adv. Mater.* **2019**, *31*, e1903125.
- [31] Y. Liu, L.-Z. Fan, L. Jiao, *J. Mater. Chem. A* **2017**, *5*, 1698–1705.
- [32] D. Liu, L. Yang, Z. Chen, G. Zou, H. Hou, J. Hu, X. Ji, *Sci. Bull.* **2020**, *65*, 1003–1012.
- [33] W. Zhan, M. Zhu, J. Lan, H. Wang, H. Yuan, X. Yang, G. Sui, *Chem. Eng. J.* **2021**, *408*, 128007.
- [34] H. Zhai, H. Jiang, Y. Qian, X. Cai, H. Liu, Y. Qiu, M. Jin, F. Xiu, X. Liu, L. Lai, *Mater. Chem. Phys.* **2020**, *240*, 122139.
- [35] C. Lu, Z. Sun, L. Yu, X. Lian, Y. Yi, J. Li, Z. Liu, S. Dou, J. Sun, *Adv. Energy Mater.* **2020**, *10*, 2001161.
- [36] W. Chen, X. Zhang, L. Mi, C. Liu, J. Zhang, S. Cui, X. Feng, Y. Cao, C. Shen, *Adv. Mater.* **2019**, *31*, e1806664.
- [37] T. Wu, C. Zhang, H. Hou, P. Ge, G. Zou, W. Xu, S. Li, Z. Huang, T. Guo, M. Jing, X. Ji, *Adv. Funct. Mater.* **2018**, *28*, 1705744.
- [38] K. T. Chen, H. Y. Tuan, *ACS Nano* **2020**, *14*, 11648–11661.
- [39] M. Kong, Y. Liu, B. Zhou, K. Yang, J. Tang, P. Zhang, W. H. Zhang, *Small* **2020**, *16*, e2001976.
- [40] P. Li, L. Yu, S. Ji, X. Xu, Z. Liu, J. Liu, J. Liu, *Chem. Eng. J.* **2019**, *374*, 502–510.
- [41] L. Hu, X. Zhu, Y. Du, Y. Li, X. Zhou, J. Bao, *Chem. Mater.* **2015**, *27*, 8138–8145.
- [42] K. Song, C. Liu, L. Mi, S. Chou, W. Chen, C. Shen, *Small* **2021**, *17*, e1903194.
- [43] K. Song, J. Liu, H. Dai, Y. Zhao, S. Sun, J. Zhang, C. Qin, P. Yan, F. Guo, C. Wang, Y. Cao, S. Li, W. Chen, *Chem* **2021**, *7*, 2684–2694.
- [44] Z. Liu, H. Sun, X. Wang, Z.-Y. Gu, C. Xu, H. Li, G. Zhang, Y. He, X.-L. Wu, *Energy Storage Mater.* **2022**, *48*, 90–100.
- [45] K. Cao, H. Liu, Y. Jia, Z. Zhang, Y. Jiang, X. Liu, K. J. Huang, L. Jiao, *Adv. Mater. Technol.* **2020**, *5*, 2000199.
- [46] B. Kong, L. Zu, C. Peng, Y. Zhang, W. Zhang, J. Tang, C. Selomulya, L. Zhang, H. Chen, Y. Wang, Y. Liu, H. He, J. Wei, X. Lin, W. Luo, J. Yang, Z. Zhao, Y. Liu, J. Yang, D. Zhao, *J. Am. Chem. Soc.* **2016**, *138*, 16533–16541.
- [47] J. Liu, L. Yu, C. Wu, Y. Wen, K. Yin, F. K. Chiang, R. Hu, J. Liu, L. Sun, L. Gu, J. Maier, Y. Yu, M. Zhu, *Nano Lett.* **2017**, *17*, 2034–2042.
- [48] X. Yang, R. Zhang, *J. Alloys Compd.* **2020**, *834*, 155191.
- [49] C. Kang, S. Zhou, J. Liu, Y. Zhu, A. Hu, Q. Tang, Y. Zhang, X. Chen, T. Tao, *J. Mater. Chem. A* **2021**, *9*, 2152–2160.
- [50] J. Z. Guo, P. F. Wang, X. L. Wu, X. H. Zhang, Q. Yan, H. Chen, J. P. Zhang, Y. G. Guo, *Adv. Mater.* **2017**, *29*, 1701968.
- [51] Y. Liu, Y. Fang, Z. Zhao, C. Yuan, X. W. D. Lou, *Adv. Energy Mater.* **2019**, *9*, 1803052.
- [52] D. Zhao, S. Jiang, S. Yu, J. Ren, Z. Zhang, S. Liu, X. Liu, Z. Wang, Y. Wu, Y. Zhang, *Carbon* **2023**, *201*, 864–870.
- [53] D. Zhao, S. Ge-Zhang, Z. Zhang, H. Tang, Y. Xu, F. Gao, X. Xu, S. Liu, J. Zhou, Z. Wang, Y. Wu, X. Liu, Y. Zhang, *ACS Appl. Mater. Interfaces* **2022**, *14*, 54662–54669.
- [54] D. Zhao, Z. Zhang, J. Ren, Y. Xu, X. Xu, J. Zhou, F. Gao, H. Tang, S. Liu, Z. Wang, D. Wang, Y. Wu, X. Liu, Y. Zhang, *Chem. Eng. J.* **2023**, *451*, 138882.
- [55] F. Gao, B. Mei, X. Xu, J. Ren, D. Zhao, Z. Zhang, Z. Wang, Y. Wu, X. Liu, Y. Zhang, *Chem. Eng. J.* **2022**, *448*, 137742.

Manuscript received: January 17, 2023

Revised manuscript received: March 14, 2023

Accepted manuscript online: March 18, 2023

Version of record online: April 12, 2023